

## Nickel Nanowire Arrays with Preferential Orientation for Boosting Hydrogen Evolution Reaction Capability

To cite this article: Xuanxuan Feng *et al* 2020 *J. Electrochem. Soc.* **167** 106501

View the [article online](#) for updates and enhancements.

### You may also like

- [Controlling Optical Properties of Aluminum Oxide Using Electrochemical Deposition](#)  
Hao Ming Chen, Chia Fen Hsin, Ru-Shi Liu *et al.*
- [Concluding remarks](#)  
R R Betts
- [Halbach array assisted assembly of orderly aligned nickel nanowire networks as transparent conductive films](#)  
Jie Wang, Shumin Liu, Chaolei Ban *et al.*



### Your Lab in a Box!

The PAT-Tester-i-16: All you need for Battery Material Testing.

- ✓ All-in-One Solution with integrated Temperature Chamber!
- ✓ Cableless Connection for Battery Test Cells!
- ✓ Fully featured Multichannel Potentiostat / Galvanostat / EIS!

[www.el-cell.com](http://www.el-cell.com) +49 40 79012-734 [sales@el-cell.com](mailto:sales@el-cell.com)

  
electrochemical test equipment





# Nickel Nanowire Arrays with Preferential Orientation for Boosting Hydrogen Evolution Reaction Capability

Xuanxuan Feng, Shaokang Bian, Na Wang, Fan Wang, Hongxin Guan, Xianfeng Hao, Mengnan Ma, Xuesen Gao, and Yan Chen<sup>z</sup>

Key Laboratory of Applied Chemistry, College of Environmental and Chemical Engineering, Yanshan University, Qinhuangdao 066004, People's Republic of China

Nickel nanowire arrays with preferential growth of (111), (200) and (220) lattice planes were prepared via a modified template-assisted electrodeposition method respectively. As a HER electrocatalyst, (220) preferred orientation nickel nanowire arrays exhibited higher catalytic activity and stability in alkaline solution, and the hydrogen evolution overpotential was as low as 128 mV at the current density of 10 mA · cm<sup>-2</sup>. The performance is attributed to the higher surface energy of the (220) lattice plane of nickel nanowire arrays as the exposed surface and more active sites participate in HER process, which is beneficial to charge transfer and decrease of activation energy of reactions. Simultaneously, the activation energy of exposed surface evaluated directly by calculating with First-principles correspond to the trend of the experimental results, catalytic activity (220) > (200) > (111) lattice plane in the hydrogen evolution process. The strategy of using crystal anisotropy to improve catalytic performance can be extended to the synthesis of other nanocrystals with higher activity and high-energy surface catalysts.

© 2020 The Electrochemical Society ("ECS"). Published on behalf of ECS by IOP Publishing Limited. [DOI: 10.1149/1945-7111/ab9756]

Manuscript submitted January 9, 2020; revised manuscript received April 4, 2020. Published June 5, 2020.

The future energy demand shows that hydrogen energy is regarded as the most ideal energy carrier.<sup>1</sup> It has the advantages of high calorific value, no pollution of products and abundant sources.<sup>2,3</sup> Electrolytic water is widely recognized as a promising and sustainable method for producing clean hydrogen fuels.<sup>4,5</sup> Electrocatalytic hydrogen evolution reaction is a vital step in the process of water split, due to its slow kinetics process in alkaline solution, the exploit of highly efficient HER electrocatalysts is imminent.<sup>6</sup> To further improve the hydrogen evolution performance of existing non-platinum catalysts is the key to achieve large-scale production of electrolyzed water.

In recent years, as a promising substitute for precious metal platinum, the metal catalysts enriched on earth has been extensively studied. Nickel has high activity and abundant reserves, so it has become one of the coking substitutes for hydrogen evolution catalysts. In order to achieve the purpose of nickel material to compete with precious metals, the electronic structure of the catalysts can be changed through the synergy between the elements,<sup>7</sup> which can improve the charge transfer efficiency. Researchers have prepared complex compounds by combining metallic nickel and non-metallic elements to improve the reactivity and electrochemical stability of metals.<sup>8-12</sup> For example, combining chalcogens with metallic nickel (such as NiS<sub>2</sub>, Ni<sub>3</sub>S<sub>3</sub>, Ni-Co, Ni-P, Ni<sub>x</sub>P/S/Se-Co<sub>x</sub>P/S/Se, etc.<sup>1,13-16</sup>) can further enhanced the electrocatalytic activity of nickel-base material. Compared with pure nickel nanostructures, the novel catalyst has excellent electrocatalytic performance. On the other hand, increasing the surface roughness to increase the specific surface area, for example, metal nickel is made into nanowires, nanosheets or nanoparticles,<sup>17-21</sup> etc., and the catalytic performance is better than nickel plating. However, nanomaterials are prone to agglomeration or clustering due to their special properties, which reduces the specific surface area of the catalysts. Using three-dimensional structure substrates with different substrates (such as nickel foam, carbon cloth,<sup>22,23</sup> etc.) can effectively disperse nanomaterials or increase their surface area by stacking nanoscale structures.<sup>23</sup> Furthermore, the catalytic material growth directly on the three-dimensional substrate can avoid the use of the binder, which increases the electrical conductivity of the material and reduces the error in measuring the resistance.

From a crystallographic point of view, for nickel metal, the energy of (220) crystal plane of nickel is higher than the (200) and (111) lattice planes of nickel. According to the anisotropy of the

crystal plane, exposing the high-energy crystal plane and optimizing the adsorption energy of the intermediate to increase the number of active sites can improve the catalytic performance of the material. A method of distinguishing the catalytic properties of elemental metals by crystal plane anisotropy has rarely been mentioned.

This work focuses on the anisotropy of nickel nanowire arrays for the catalytic activity of HER. Three-dimensional nickel nanowire arrays with different crystal plane preferential orientations was successfully manufactured by using a titanium plate as a substrate and using AAO template-assisted potentiostatic electrodeposition. And the influence of the nickel nanowire arrays with preferential orientation on three lattice planes on the HER performance was studied. Different lattice planes resulted in energy differences between hydrogen and hydroxyl species and further affects the energy barrier of the initial water dissociation step. The different crystal surface energies and the hydrogen adsorption/desorption energy in the HER process were calculated by density functional theory. This provides a feasible reference for the in-depth research and application of nickel-based electrocatalysts or other metal catalysts.

## Experimental

**Synthesis of different crystal plane Ni nanowires arrays.**—The AAO templates were prepared using a typical two-step anodic oxidation method based on previously reported literature.<sup>24</sup> Ni nanowire arrays were synthesized by employing electrodeposition method in a three-electrode system. The working electrode was assembled sequentially a titanium sheet (~150 μm thickness) as substrate, the through-hole AAO template, and a nickel foam. The saturated calomel electrode (SCE) and platinum film (2 cm × 2 cm × 0.01 cm) was used as reference electrode and counter electrode, respectively. The basic composition of the electrolyte was NiSO<sub>4</sub> · 6H<sub>2</sub>O (30 g), NiCl<sub>2</sub> · 6H<sub>2</sub>O (4.5 g), and H<sub>3</sub>BO<sub>3</sub> (4.5 g) dissolving in deionized water (120 ml) and the obtained electrolyte pH was 3.7. The preferred orientation of the (111) crystal plane of nickel was recorded as Ni<sub>(111)</sub> with a deposition voltage of -0.8 V at 20 °C. Similarly, Ni<sub>(200)</sub> had a deposition voltage of -1.0 V, a pH of 2.2 with being controlled by dilute sulfuric acid at 60 °C and NH<sub>4</sub>F was added to make Ni<sup>2+</sup>:NH<sub>4</sub>F = 8:1 and Ni<sub>(220)</sub> was deposited at -1.2 V and at 35 °C. The different crystal plane Ni nanowire arrays that attached to the Ti substrate was moved the AAO template in 5 wt% NaOH and dried at room temperature for further characterization.

<sup>z</sup>E-mail: chenyan@ysu.edu.cn

**Materials characterization.**—Crystal structure of the samples was analyzed by using powder X-ray diffractometer (XRD, RigakuD/MAX-2500/PC) with Cu K $\alpha$  radiation ( $\lambda = 1.5418 \text{ \AA}$ ). The morphology and chemical composition were obtained by scanning electron microscopy (SEM, Zeiss Supra 55, 15 keV) with energy dispersive spectrometer (EDS) and a transmission electron microscope (TEM, Tecnai T20 G2).

**Electrochemical measurements.**—Electrochemical measurements were executed at room temperature with a CHI 660E electrochemical workstation (Chen Hua Instruments, Shanghai) in a typical three-electrode system. The nanowire arrays attached to the Ti substrate were directly used as working electrode without any further treatment, platinum sheet ( $1 \text{ cm} \times 1 \text{ cm} \times 0.01 \text{ cm}$ ) as counter electrode and an Hg/HgO electrode as the reference electrode in 1 M KOH. Line scan voltammetry (LSV) curves were performed at a sweep rate of  $5 \text{ mV} \cdot \text{s}^{-1}$ . All LSV data were presented with current normalization and  $iR$  compensation. Electrochemical impedance spectroscopy (EIS) was executed from 100 kHz to 0.01 Hz with an AC voltage amplitude of 5 mV. The chronoamperometry tests were performed at a constant potential of  $-1.155 \text{ V}$  vs Hg/HgO for 35 h. CV was carried out from  $-0.9 \text{ V}$  to  $-1.35 \text{ V}$  (vs Hg/HgO) at a rate of  $50 \text{ mV} \cdot \text{s}^{-1}$  for 2500 cycles in order to test the durability of the catalyst. All the current densities were normalized using the geometrical area of the working electrodes. Reversible hydrogen electrode (RHE) scale was calculated by Eq. 1:

$$E_{\text{RHE}} = E_{\text{Hg/HgO}} + 0.05916 \text{ pH} + E_{\text{Hg/HgO}}^{\ominus} \quad [1]$$

Where,  $E_{\text{RHE}}$  was the converted potential vs RHE,  $E_{\text{Hg/HgO}}$  was the potential measured in the experiment against the Hg/HgO reference electrode, and  $E_{\text{Hg/HgO}}^{\ominus}$  was the standard potential of Hg/HgO at  $25 \text{ }^{\circ}\text{C}$  ( $0.098 \text{ V}$ ).

**Density functional theory (DET) calculation.**—First-principles calculations was performed by using the Vienna ab initio Simulation Package (VASP).<sup>25,26</sup> All density functional calculations were conducted using the projector-augmented plane-wave (PAW) method<sup>27,28</sup> within GGA-PBE exchange correlation functional.<sup>27</sup> The cutoff energy of plane wave was set to 400 eV. Relaxation was permitted until the atomic force was below  $-0.01 \text{ eV } \text{\AA}^{-1}$  and the change of the energy was below 0.1 meV.

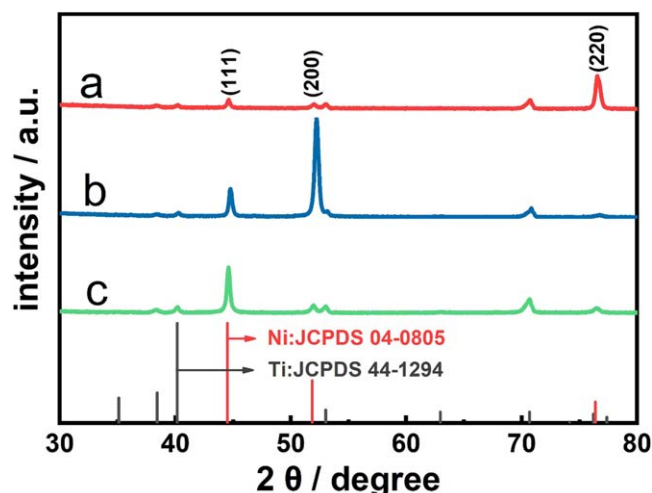


**Figure 1.** XRD patterns of the as-synthesized (a) Ni<sub>(220)</sub>; (b) Ni<sub>(200)</sub>; (c) Ni<sub>(111)</sub>.

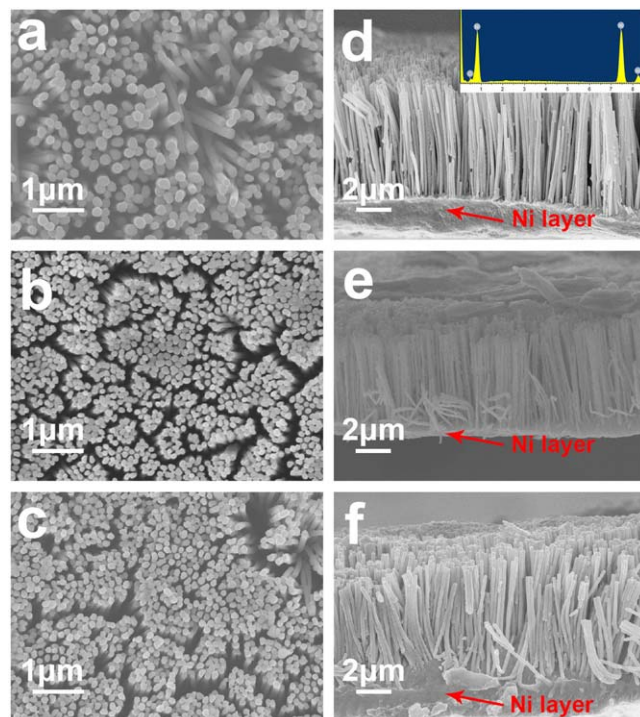


**Figure 2.** The SEM images of Ni nanowires with different lattice plane orientations (a) (d) Ni<sub>(111)</sub>, the inset in (b) was the EDS spectrum of Ni layer; (b) (e) Ni<sub>(200)</sub>; (c) (f) Ni<sub>(220)</sub>.

The free energies were evaluated as Eq. 2:

$$\Delta G(H^*) = \Delta E(H^*) + \Delta \text{ZPE} - T\Delta S \quad [2]$$

where  $\Delta E(H^*)$ ,  $\Delta \text{ZPE}$  and  $\Delta S$  were the binding energy, zero point energy change and entropy change of H\* adsorption, respectively.

$\Delta S$  was obtained by the Eq. 3, in view of the negligible vibrational entropy of H\*.

$$\Delta S = S(H^*) - 1/2 S(H_2) \approx -1/2 S(H_2) \quad [3]$$

The corresponding  $T\Delta S$  was  $-0.205 \text{ eV}$ , since  $TS(H_2)$  was known to be  $0.41 \text{ eV}$  for H<sub>2</sub> at 300 K and 1 atm.

$$\Delta \text{ZPE} = \text{ZPE}(H^*) - 1/2 \text{ZPE}(H_2) \quad [4]$$

$\text{ZPE}(H_2)$  value was calculated about  $0.327 \text{ eV}$ ,  $\text{ZPE}(H^*) = 0.114$ .

So the final formula turned to Eq. 5

$$\Delta G(H^*) = \Delta E(H^*) + 0.155 \quad [5]$$

## Results and Discussion

XRD was used to characterize Ni nanowires with different crystal plane orientations. Besides the peaks from Ti substrate, the other three characteristic diffraction peaks located at  $2\theta$  values of  $44.51^\circ$ ,  $51.85^\circ$  and  $76.37^\circ$  corresponded to the (111), (200) and (220) lattice planes of face-centered cubic phase of Ni (JCPDS No. 04-0805). Fig. 1. exhibited the XRD pattern of Ni nanowires in different deposition conditions. From Fig. 1c, at  $-0.8 \text{ V}$  and  $20 \text{ }^{\circ}\text{C}$ , the ratio of the peak intensity of the obtained nickel nanowire arrays was (111): (200): (220) = 4.8: 1.3: 1, compared with the JCPDS No. 04-0805 (the peak intensity ratio is (111): (200): (220) = 4.7: 2: 1). It can be seen that the (111) lattice plane of nickel nanowire arrays grown preferentially. Similarly, when the deposition voltage and temperature were increased, as shown in Fig. 1a, the ratio of peak intensity was (111): (200): (220) = 0.4: 0.3: 1 which illustrate the

(220) lattice plane grown preferentially. Figure 1b showed the peak intensity ratio of the three lattice planes of was (111):(200):(220) = 4.3: 13: 1, implying (200) lattice plane grown preferentially after adjusting the deposition voltage, pH and temperature and adding fluoride ions.<sup>29</sup>

Metal nickel had a face-centered cubic (FCC) structure, and the lattice plane energy tended to decrease in the order of (110) ( $1.98 \text{ J} \cdot \text{cm}^{-2}$ ), (100) ( $1.76 \text{ J} \cdot \text{cm}^{-2}$ ), and (111) ( $1.63 \text{ J} \cdot \text{cm}^{-2}$ ).<sup>30</sup> At lower temperatures ( $T = 20 \text{ }^\circ\text{C}$ ) and deposition voltage ( $V = -0.8 \text{ V}$ ), Ni grew preferentially along the lowest crystal plane energy (111) due to the confinement effect of AAO template. As the deposition voltage gradually increased, the deposition rate of Ni was accelerated. The growth direction of highest crystal plane energy (220) was consistent with the current direction and will be developed with priority and the other crystal planes were covered under the constraint of nanopores. The (200) lattice plane was dominant owing the presence of  $\text{F}^-$ , which had a strong electrochemical adsorption effect on (111) and (110) lattice planes and to the lowered pH (2.2).<sup>31,32</sup>

The morphology of the  $\text{Ni}_{(111)}$ ,  $\text{Ni}_{(200)}$  and  $\text{Ni}_{(220)}$  were showed in Fig. 2., the diameter of the nanowires was about 100 nm, which was in agreement with the pore size of the AAO template. The length of the nickel nanowires was controlled to be around  $5 \mu\text{m}$  and the Ni nanowire arrays were grown vertically along the AAO template pore on the substrate. The side view of the SEM diagram (Figs. 2d–2f) revealed that a deposition layer was formed between the nickel nanowires and the Ti substrate. It can be seen from the EDS analysis of the illustration in Fig. 2d that the layer was metallic nickel. The reason for the nickel layer was that during the electrodeposition process, a gap exists between the AAO template and the Ti substrate, and nickel was preferentially deposited in the interstitial region and then grown along the nanopore. The nanowires could tightly bond to the Ti substrate to avoid nanowires falling off during the electrochemical test attribute to this thin nickel layer.

HER catalytic performance of different lattice plane Ni nanowire arrays was firstly investigated by linear sweep voltammetry (LSV) with  $iR$ -corrected in alkaline solution (1M KOH), showed in Fig. 3a. In order to eliminate the influence of the substrate, the Ti substrate was also subjected to LSV test. As can be seen from the Fig. 3a, the Ti substrate had almost no effect on HER. The overpotential for the  $\text{Ni}_{(220)}$  nanowires were 128, 207 and 251 mV at a geometric current density of 10, 60 and  $100 \text{ mA} \cdot \text{cm}^{-2}$  vs RHE respectively. In contrast, the overpotentials required to drive the cathodic current densities of 10, 60 and  $100 \text{ mA} \cdot \text{cm}^{-2}$  are 176, 251 and 286 mV for  $\text{Ni}_{(200)}$  nanowires and 214, 295 and 330 mV for  $\text{Ni}_{(111)}$  nanowires. Compared with other catalysts (as shown in Table I),  $\text{Ni}_{(220)}$  can improve effectively the hydrogen evolution performance of materials under alkaline conditions, which can be comparable to other composite hydrogen evolution catalysts.

The HER kinetic of Ni nanowires catalysts were illustrated by the Tafel slope that was analyzed from polarization curves depended on the Tafel equation ( $\eta = b \times \log j + a$ , where  $\eta$ ,  $b$  and  $j$  are overpotential, Tafel plots and current density). As shown in Fig. 3b, the Tafel slope of the  $\text{Ni}_{(220)}$  nanowires was  $70 \text{ mV} \cdot \text{dec}^{-1}$ , which was much lower than those of  $\text{Ni}_{(200)}$  ( $82 \text{ mV} \cdot \text{dec}^{-1}$ ) and  $\text{Ni}_{(111)}$  ( $93 \text{ mV} \cdot \text{dec}^{-1}$ ). The lower Tafel slope of the  $\text{Ni}_{(220)}$  nanowires indicated (220) the preferential orientation of the Ni nanowire arrays had fast electron transport rates and excellent hydrogen evolution kinetics. The mechanism of HER in the alkaline solution on the surface of the metal material electrode mainly includes the following three basic steps: (1) Volmer reaction:  $\text{H}_2\text{O} + \text{e}^- \rightarrow \text{H}_{\text{ads}} + \text{OH}^-$ , (2) Heyrovsky reaction:  $\text{H}_{\text{ads}} + \text{H}_2\text{O} + \text{e}^- \rightarrow \text{H}_2 + \text{OH}^-$ , and/or (3) Tafel reaction:  $\text{H}_{\text{ads}} + \text{H}_{\text{ads}} \rightarrow \text{H}_2$ , the Tafel slopes of corresponding steps are 120, 40, and  $30 \text{ mV} \cdot \text{dec}^{-1}$ , respectively.<sup>40,41</sup> The slope of  $70 \text{ mV} \cdot \text{dec}^{-1}$  for  $\text{Ni}_{(220)}$  nanowires indicated that the rate determining step could be the Heyrovsky process in alkaline condition.<sup>2</sup> To investigate the kinetics of the interface between the electrode material and the electrolyte at the HER process, the EIS was tested at 1 M KOH solution at the

overpotential corresponding to the current density of  $10 \text{ mA} \cdot \text{cm}^{-2}$ . The charge transfer resistance ( $R_{\text{ct}}$ ) was mainly determined by the diameter of the semicircle in the Nyquist plots. The result was obvious from the Fig. 3c that the charge transfer resistance ( $R_{\text{ct}}$ ) of  $\text{Ni}_{(220)}$  nanowires was only  $22.1 \Omega$ . The  $\text{Ni}_{(220)}$  nanowires exhibited the smaller  $R_{\text{ct}}$  than  $\text{Ni}_{(200)}$  and  $\text{Ni}_{(111)}$  nanowires, which revealed small electrochemical impedance promotes electron transfer to ensure rapid reaction in hydrogen evolution reaction. The absence of Warburg elements in the equivalent circuit diagram may be due to the kinetic control of the reaction process rather than the mass transfer control in the low frequency region.<sup>2</sup> The development of highly active and highly stable electrocatalysts was critical to the hydrogen evolution process and stability was an important parameter in the catalytic process. As shown in Fig. 3d, the stability of catalyst was tested by chronoamperometry and current density of  $\text{Ni}_{(220)}$  nanowire maintained at  $6 \text{ mA} \cdot \text{cm}^{-2}$  for 35 h. After 2500 cycles of the  $\text{Ni}_{(220)}$  nanowires, the polarization curve was similar to the original, which proved that the HER performance of the nickel nanowire arrays was hardly changed.

The exchange current density  $j_0$  corresponds to the exchange of current at the electrode interface at  $\eta = 0$ . Since no overpotential is applied, the value of  $j_0$  which can be obtained by linear extrapolation based on the Tafel equation ( $\eta = b \times \log(j/j_0)$ ) largely depends on the reaction activation energy of the surface of the electrocatalyst.  $\text{Ni}_{(220)}$  had a high  $j_0$  ( $151 \mu\text{A} \cdot \text{cm}^{-2}$ ) and was larger than that of  $\text{Ni}_{(200)}$  ( $87 \mu\text{A} \cdot \text{cm}^{-2}$ ) and  $\text{Ni}_{(111)}$  ( $139 \mu\text{A} \cdot \text{cm}^{-2}$ ), indicating the preferable catalytic activity of the  $\text{Ni}_{(220)}$  catalysts. The above results indicated that more exposure of the (220) lattice plane would greatly increase the catalytic activity. The electrochemically effective surface area (ECSA) was further demonstrated by electrochemically measuring the electric double layer capacitance ( $C_{\text{dl}}$ ). The active surface area was proportional to the capacitance, and the larger the  $C_{\text{dl}}$ , the larger the surface area of the catalyst under investigation. The slope obtained by the following formula  $C_{\text{dl}} = j/v$  is the electric double layer capacitance. The relationship between the scanning rate from  $100 \text{ mV} \cdot \text{s}^{-1}$ – $500 \text{ mV} \cdot \text{s}^{-1}$  and the current density was obtained by cyclic voltammetry (CV). The ECSA of the  $\text{Ni}_{(220)}$  catalyst was  $3.18 \text{ mF} \cdot \text{cm}^{-2}$ , which was higher than those of  $\text{Ni}_{(200)}$  ( $1.79 \text{ mF} \cdot \text{cm}^{-2}$ ),  $\text{Ni}_{(111)}$  ( $0.402 \text{ mF} \cdot \text{cm}^{-2}$ ). The data indicated that  $\text{Ni}_{(220)}$  with higher lattice plane energy would expose more active sites to promote hydrogen evolution reaction.

To further explore the stability of Ni nanowire array in hydrogen evolution, the  $\text{Ni}_{(220)}$  before and after electrochemical tests were characterized by TEM. As shown in Fig. 4, the catalyst still maintained the nanowire morphology after the test, the surface of Ni nanowires appeared one more thin film than before the test. However, XRD characterization of  $\text{Ni}_{(220)}$  after test (Fig. 5) showed that no obvious nickel hydroxide or oxide peaks presented, which may be sparse and below the detection limit and also further showed that  $\text{Ni}_{(220)}$  had excellent structure stability as a HER catalyst. Since the HER test was executed under alkaline conditions, it can be concluded that the film was nickel hydroxide.<sup>18,42</sup> The few amount of nickel hydroxide on the top and side surface facilitated the transfer of electrons between nickel and nickel ions. Furthermore, the good morphology and structure stability of the Ni nanowire was conducive to transfer electrons from the correct collector to the reaction sites through each individual nanowire with high efficacy and also was beneficial to avoid the collapse of the framework during the hydrogen escape. Based on the lattice plane energy, the lattice plane energy of (220) was higher and it was easier to form nickel hydroxides, displayed highest intrinsic activity among the Ni nanowire arrays with preferential growth of (111), (200) and (220) lattice planes.

To describe the performance of hydrogen evolution in a finer way, the first-principles calculations were performed. It was well-known that the free energy of adsorption ( $\Delta G_{\text{H}^*}$ ) of H was an excellent indicator for the HER catalyst, and  $\Delta G_{\text{H}^*} \approx 0$  indicates a high catalytic activity.<sup>43</sup> As presented in Fig. 6, hydrogen adsorption/desorption on (100), (111) and (110) surfaces of Ni were

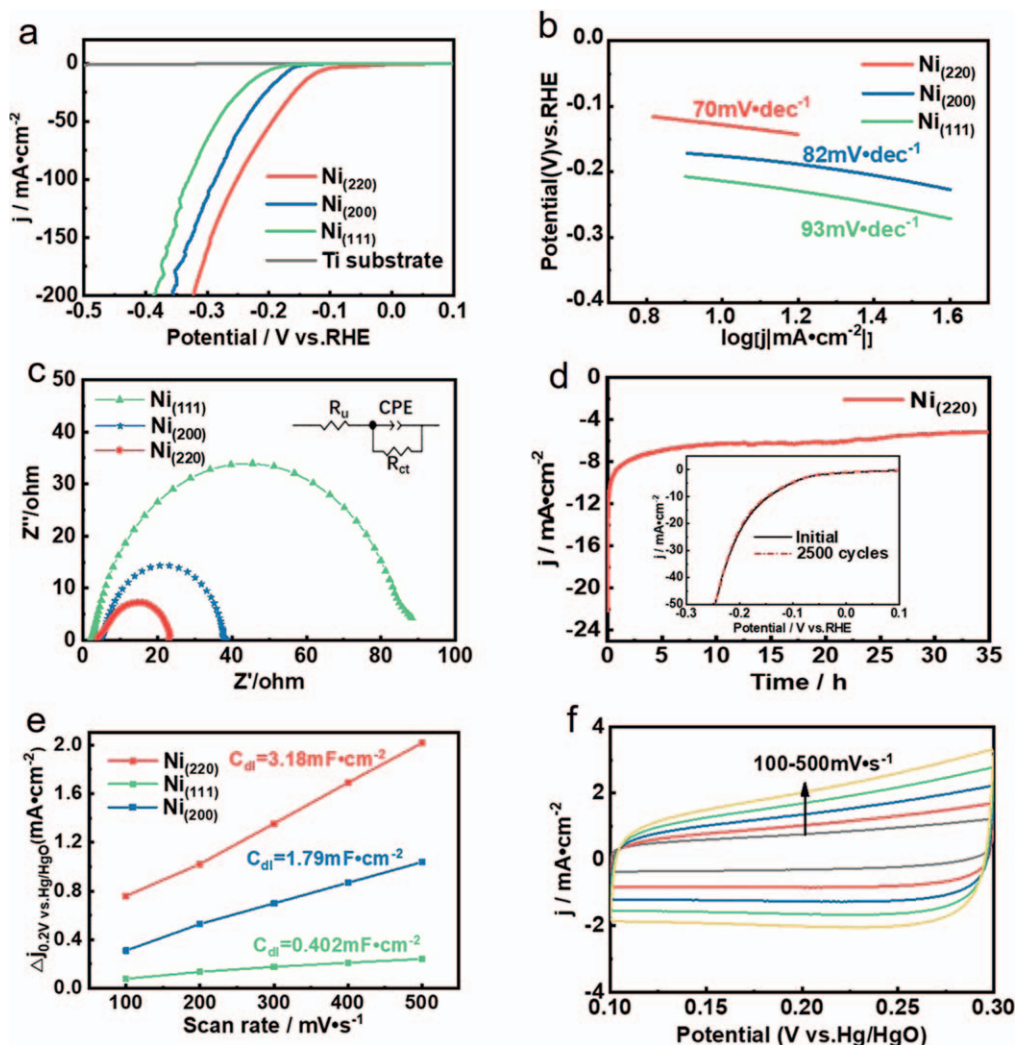


**Figure 3.** (a). Polarization curves of Ti substrate, Ni<sub>(220)</sub>, Ni<sub>(200)</sub>, and Ni<sub>(111)</sub>. (b). Tafel curves of Ni<sub>(220)</sub>, Ni<sub>(200)</sub>, and Ni<sub>(111)</sub>. (c). Corresponding electrochemical impedance spectroscopy (EIS) Nyquist plots of different catalysts. (d). Chronoamperometric measurement of the Ni<sub>(220)</sub> at a constant potential of  $-1.155$  V. Inset is the polarization curves of the Ni<sub>(220)</sub> before and after 2500 CV cycles. (e). Linear fitting of the capacitive currents versus CV scan rates for the different catalysts; (f). CV curves of Ni<sub>(220)</sub> in the non-Faradaic capacitance current range at scan rates from 100 to 500  $\text{mV} \cdot \text{s}^{-1}$ .

**Table I.** Performance comparison of various nickel-based catalysts for HER in alkaline solutions has been reported in the past five years.

Catalyst	Electrolyte	Current density	Overpotential	References
Ni-Co-NiCoO <sub>4</sub>	1 M KOH	10 $\text{mA} \cdot \text{cm}^{-2}$	125 mV	6
Ni <sub>3</sub> S <sub>2</sub>	1 M KOH	10 $\text{mA} \cdot \text{cm}^{-2}$	199 mV	33
		30 $\text{mA} \cdot \text{cm}^{-2}$	258.4 mV	
Co <sub>3</sub> O <sub>4</sub> @Ni	1 M KOH	10 $\text{mA} \cdot \text{cm}^{-2}$	225 mV	34
NiCo <sub>2</sub> O <sub>4</sub> -MCNTs	0.1 M KOH	10 $\text{mA} \cdot \text{cm}^{-2}$	209 mV	35
MoS <sub>2</sub> @NiO	1 M KOH	10 $\text{mA} \cdot \text{cm}^{-2}$	406 mV	36
CuO@Ni/NiFe	1 M KOH	10 $\text{mA} \cdot \text{cm}^{-2}$	125 mV	37
Ni <sub>2</sub> P	1 M KOH	20 $\text{mA} \cdot \text{cm}^{-2}$	205 mV	13
ZnNi-P/NSs	1 M KOH	10 $\text{mA} \cdot \text{cm}^{-2}$	175 mV	38
		50 $\text{mA} \cdot \text{cm}^{-2}$	291 mV	
NiCo-LDH/NF	1 M KOH	10 $\text{mA} \cdot \text{cm}^{-2}$	168 mV	39
Ni <sub>(220)</sub>	1 M KOH	10 $\text{mA} \cdot \text{cm}^{-2}$	128 mV	This work
		60 $\text{mA} \cdot \text{cm}^{-2}$	207 mV	This work

calculated with respect to configurations of three hydrogen adsorption sites, including top site, bridge site and hollow site. The hollow site of Ni<sub>(110)</sub> showed the smallest  $|\Delta G_{\text{H}^*}|$  value of 0.058 eV, which

was close to the optimum value and was highly reactive. The higher values of Ni<sub>(100)</sub> ( $|\Delta G_{\text{H}^*}| = 0.180$  eV) and Ni<sub>(111)</sub> ( $|\Delta G_{\text{H}^*}| = 0.215$  eV) hindered the adsorption of water and H active

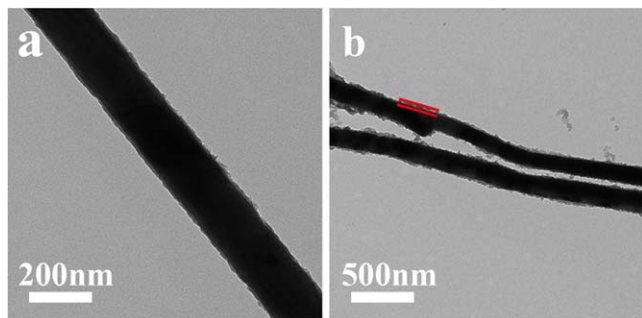


**Figure 4.** TEM images of Ni<sub>(220)</sub>: Before (a) and After (b) electrochemical test.

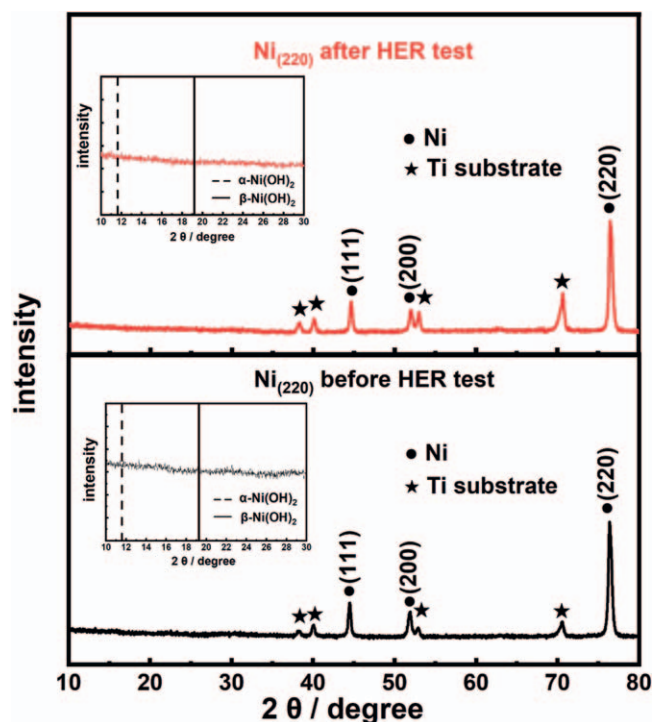


**Figure 5.** XRD spectrum of Ni<sub>(220)</sub> before and after electrochemical test.

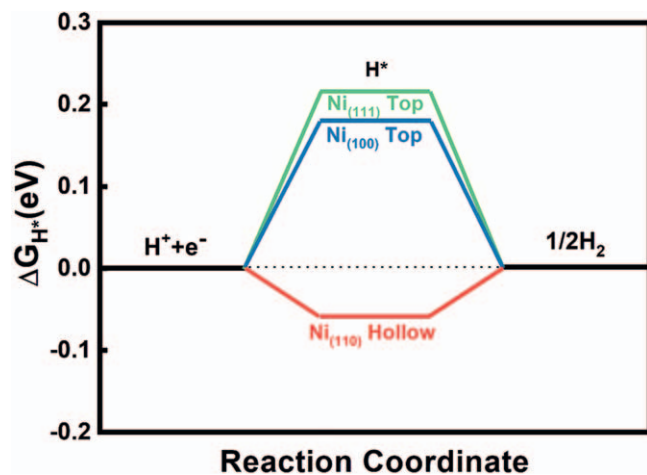


**Figure 6.** The corresponding free energy diagram for HER on the different crystal faces of nickel nanowires array.

intermediates, resulting in slow kinetics. Consistent with experimental data that the HER performance of the Ni nanowire arrays

tended to decrease in the order of the (110), (100), and (111) lattice planes. The Ni<sub>(220)</sub> had a higher lattice plane energy, and the total energy of adsorption and desorption of hydrogen by the (220) of nickel was lower, resulting in a reduction of the initial water decomposition step and subsequent generation and escape of hydrogen barrier. Simultaneously, the nanostructures exposed more active catalytic sites and optimized hydrogen adsorption and desorption. Ni<sub>(220)</sub> were directly grown on the Ti substrate as working electrodes, so there was no contact resistance between them, and good electrical conductivity to promote electron transfer between the catalyst and the electrode. These advantages play an active role in enhancing the catalytic performance.

## Conclusions

Ni nanowire arrays with preferential growth on different lattice planes were prepared by AAO template-assisted method. Compared to the (200) and (111) lattice planes of nickel, Ni<sub>(220)</sub> only demanded 128 mV overpotential to drive the current density of 10 mA · cm<sup>-2</sup>. According to the anisotropy of the lattice plane of nickel metal, the high-energy lattice plane was more exposed, the morphological characteristics of three-dimensional nanowire arrays avoided the aggregation of nanomaterials, and the active sites that can be adsorbed by hydrogen intermediates increased, which was the main reason for improving HER performance. Combined with theoretical calculations, the high-energy lattice plane of nickel, had a lower Gibbs free energy ( $\Delta G = -0.058$  eV) during HER process. The strategy of growing metal high-energy lattice planes to improve the electrocatalytic performance has great potential in the field of catalysis which can provide valuable information for the rational design of metal-based HER catalyst.

## ORCID

Yan Chen <https://orcid.org/0000-0002-6053-8422>

## References

- W. Q. Tang, J. Y. Wang, and L. X. Gu, "Heterostructured arrays of Ni<sub>3</sub>P/Se Nanosheets on CoxP/S/Se nanowires for efficient hydrogen evolution[J]." *ACS Appl. Mater. Interfaces*, **9**, 41347 (2017).
- D. L. Jiang, W. X. Ma, and Y. M. Zhou, "Coupling Co<sub>2</sub>P and CoP nanoparticles with copper ions incorporated Co<sub>9</sub>S<sub>8</sub> nanowire arrays for synergistically boosting hydrogen evolution reaction electrocatalysis[J]." *J. Colloid and Interface Sci.*, **550**, 10 (2019).
- A. Ursua, L. M. Gandia, and P. Sanchis, "Hydrogen production from water electrolysis: current status and future trends[J]." *Proc. of the IEEE*, **100**, 410 (2012).
- W. X. Chen, Y. W. Zhang, and G. L. Chen, "Interface coupling of Ni-Co layered double hydroxide nanowires and cobalt-based zeolite organic frameworks for efficient overall water splitting[J]." *ACS Sustainable Chem. Eng.*, **7**, 8255 (2019).
- X. Jin, J. Li, and Y. T. Cui, "In-situ synthesis of porous Ni<sub>2</sub>P nanosheets for efficient and stable hydrogen evolution reaction[J]." *Int. J. Hydrog. Energy*, **44**, 5739 (2019).
- X. Y. Yang, G. L. Wang, and D. M. Zhang, "Three-dimensional Ni-Co-NiCo<sub>2</sub>O<sub>4</sub>/NF as an efficient electrode for hydrogen evolution reaction[J]." *Int. J. Hydrogen Energy*, **44**, 226 (2019).
- M. Yang, Y. M. Jiang, and S. Liu, "Regulating the electron density of dual transition metal sulfide heterostructures for highly efficient hydrogen evolution in alkaline electrolytes[J]." *Nanoscale*, **11**, 14016 (2019).
- Y. Xiong, L. L. Xu, and C. D. Jin, "Interface-engineered atomically thin Ni<sub>3</sub>S<sub>2</sub>/MnO<sub>2</sub> heterogeneous nanoarrays for efficient overall water splitting in alkaline media[J]." *Appl. Catal. B: Environ.*, **254**, 329 (2019).
- C. C. Lv, Z. Peng, and Y. X. Zhao, "The hierarchical nanowires array of iron phosphide integrated on a carbon fiber paper as an effective electrocatalyst for hydrogen generation[J]." *J. Mater. Chem. A*, **4**, 1454 (2016).
- B. Zhang, J. Liu, and J. S. Wang, "Interface engineering: the Ni(OH)<sub>2</sub>/MoS<sub>2</sub> heterostructure for highly efficient alkaline hydrogen evolution[J]." *Nano Energy*, **37**, 74 (2017).
- K. L. Liu, F. M. Wang, and K. Xu, "CoS<sub>2x</sub>Se<sub>2(1-x)</sub> nanowire array: an efficient ternary electrocatalyst for the hydrogen evolution reaction[J]." *Nanoscale*, **8**, 4699 (2016).
- J. G. Hou, Y. Q. Sun, and Z. W. Li, "Electrical behavior and electron transfer modulation of nickel-copper nanoalloys confined in nickel-copper nitrides nanowires array encapsulated in nitrogen-doped carbon framework as robust bifunctional electrocatalyst for overall water splitting[J]." *Adv. Funct. Mater.*, **28**, 1803278 (2018).

13. E. J. Popczun, J. R. McKone, and C. G. Read, "Nanostructured nickel phosphide as an electrocatalyst for the hydrogen evolution reaction[J]." *J. Am. Chem. Soc.*, **135**, 9267 (2013).
14. Q. Ma, C. Hu, and K. Liu, "Identifying the electrocatalytic sites of nickel disulfide in alkaline hydrogen evolution reaction[J]." *Nano Energy*, **41**, 148 (2017).
15. C. Yang, M. Y. Gao, and Q. B. Zhang, "In-situ activation of self-supported 3D hierarchically porous Ni<sub>3</sub>S<sub>2</sub> films grown on nanoporous copper as excellent pH-universal electrocatalysts for hydrogen evolution reaction[J]." *Nano Energy*, **36**, 85 (2017).
16. Z. Peng, D. Jia, and A. M. Al-Enizi, "From water oxidation to reduction: homologous Ni-Co based nanowires as complementary water splitting electrocatalysts[J]." *Adv. Energy Mater.*, **5**, 1402031 (2015).
17. G. X. Qv, Y. W. Zhao, and G. L. Zhao, "Ultra-high length-to-diameter ratio nickel phosphide nanowires as pH-wide electrocatalyst for efficient hydrogen evolution [J]." *Electrochim. Acta*, **298**, 943 (2019).
18. H. Ogihara, M. Fujii, and T. Saji, "Hydrogen evolution reaction (HER) over electroless-deposited nickel nanospine arrays[J]." *RSC Adv.*, **4**, 58660 (2014).
19. J. K. Le, Y. G. Yi, and H. J. Lee, "Electrocatalytic activity of Ni nanowires prepared by galvanic electrodeposition for hydrogen evolution reaction[J]." *Catal. Today*, **146**, 188 (2009).
20. W. F. Chen, K. Sasaki, and C. Ma, "Hydrogen-evolution catalysts based on non-noble metal nickel-molybdenum nitride nanosheets[J]." *Angew. Chem. Int. Ed.*, **51**, 6131 (2012).
21. S. H. Ahn, S. J. Hwang, and S. J. Yoo, "Electrodeposited Ni dendrites with high activity and durability for hydrogen evolution reaction in alkaline water electrolysis [J]." *J. Mater. Chem.*, **22**, 15153 (2012).
22. L. X. Wang, Y. Li, and M. Xia, "Ni nanoparticles supported on graphene layers: an excellent 3D electrode for hydrogen evolution reaction in alkaline solution[J]." *J. Power Sources*, **347**, 220 (2017).
23. L. N. Sha, J. L. Yin, and K. Ye, "The construction of self-supported thorny leaf-like nickel-cobalt bimetal phosphides as efficient bifunctional electrocatalysts for urea electrolysis[J]." *J. Mater. Chem. A*, **7**, 9078 (2019).
24. X. S. Gao, Y. N. Wang, and W. Li, "Free-standing ni-co alloy nanowire arrays: efficient and robust catalysts toward urea electro-oxidation[J]." *Electrochim. Acta*, **283**, 1277 (2018).
25. G. Kresse and J. Hafner, "Ab initio molecular dynamics for liquid metals[J]." *Phys. Rev. B*, **47**, 558 (1993).
26. G. Kresse and J. Hafner, "Ab initio molecular-dynamics simulation of the liquid-metal-amorphous-semiconductor transition in germanium[J]." *Phys. Rev. B*, **49**, 14251 (1994).
27. P. E. Blöchl, O. Jepsen, and O. K. Andersen, "Improved tetrahedron method for Brillouin-zone integrations[J]." *Phys. Rev. B*, **49**, 16223 (1994).
28. G. Kresse and D. Joubert, "From ultrasoft pseudopotentials to the projector augmented-wave method[J]." *Phys. Rev. B*, **59**, 1758 (1999).
29. D. P. Cai, S. H. Xiao, and D. D. Wang, "Morphology controlled synthesis of NiCo<sub>2</sub>O<sub>4</sub> nanosheet array nanostructures on nickel foam and their application for pseudocapacitors[J]." *Electrochim. Acta*, **142**, 118 (2014).
30. H. Y. Sun, X. H. Li, and Y. Chen et al., "The control of the growth orientations of electrodeposited single-crystal nanowire arrays: a case study for hexagonal CdS[J]." *Nanotechnology*, **19**, 225601 (2008).
31. M. Boubatra, A. Azizi, and G. Schmerber et al., "Morphology, structure, and magnetic properties of electrodeposited Ni films obtained from different pH solutions[J]." *J. Mater. Sci.- Mater. Electron.*, **22**, 1804 (2011).
32. T. Doi, K. Mizumoto, and S. Tanaka et al., "Effect of bath pH on nickel citrate electroplating bath[J]." *Met. Finish.*, **102**, 104 (2004).
33. J. J. Li, P. K. Shen, and Z. Q. Tian, "One-step synthesis of Ni<sub>3</sub>S<sub>2</sub> nanowires at low temperature as efficient electrocatalyst for hydrogen evolution reaction[J]." *Int. J. Hydrogen Energy*, **42**, 7136 (2017).
34. R. C. Li, D. Zhou, and J. X. Luo et al., "The urchin-like sphere arrays Co<sub>3</sub>O<sub>4</sub> as a bifunctional catalyst for hydrogen evolution reaction and oxygen evolution reaction [J]." *J. Power Sources*, **341**, 250 (2017).
35. E. Umeshbabu, P. H. K. Charan, and P. Justin et al., "Hierarchically organized NiCo<sub>2</sub>O<sub>4</sub> microflowers anchored on multiwalled carbon nanotubes: efficient bifunctional electrocatalysts for oxygen and hydrogen evolution reactions[J]." *ChemPlusChem*, **85**, 183 (2020).
36. Z. H. Ibupoto, A. Tahira, and P. Y. Tang et al., "MoS<sub>x</sub>@ nio composite nanostructures: an advanced nonprecious catalyst for hydrogen evolution reaction in alkaline media[J]." *Adv. Funct. Mater.*, **29**, 1807562 (2019).
37. Y. H. Liu, Z. Y. Jin, and X. Q. Tian et al., "core-shell copper oxide@ nickel/nickel-iron hydroxides nanoarrays enabled efficient bifunctional electrode for overall water splitting[J]." *Electrochim. Acta*, **318**, 695 (2019).
38. M. L. N. Thi, T. H. Tran, and P. D. H. Anh et al., "Hierarchical zinc-nickel phosphides nanosheets on 3D nickel foam as self-support electrocatalysts for hydrogen evolution reaction[J]." *Polyhedron*, **168**, 80 (2019).
39. J. G. Yan, L. G. Chen, and X. Liang, "Co<sub>9</sub>S<sub>8</sub> nanowires@ NiCo LDH nanosheets arrays on nickel foams towards efficient overall water splitting[J]." *Sci. Bull.*, **64**, 158 (2019).
40. B. E. Conway and B. V. Tilak, "Interfacial processes involving electrocatalytic evolution and oxidation of H<sub>2</sub>, and the role of chemisorbed H[J]." *Electrochim. Acta*, **47**, 3571 (2002).
41. L. Y. Zeng, K. Sun, and X. B. Wang, "Three-dimensional-networked Ni<sub>2</sub>P/Ni<sub>3</sub>S<sub>2</sub> heteronanoflake arrays for highly enhanced electrochemical overall-water-splitting activity[J]." *Nano Energy*, **51**, 26 (2018).
42. D. S. Hall, C. Bock, and B. R. MacDougall, "The electrochemistry of metallic nickel: oxides, hydroxides, hydrides and alkaline hydrogen evolution[J]." *J. Electrochem. Soc.*, **160**, F235 (2013).
43. Y. Zheng, Y. Jiao, and Y. H. Zhu, "Hydrogen evolution by a metal-free electrocatalyst[J]." *Nat. Commun.*, **5**, 3783 (2014).